Ultrafast exciton many-body interactions and hot-phonon bottleneck in colloidal cesium lead halide perovskite nanocrystals

Anirban Mondal,[1,*] J. Aneesh,[1,*] Vikash Kumar Ravi,[2] Rituraj Sharma,[1] Wasim J. Mir,[2] Mathew C. Beard,[3] Angshuman Nag,[2,4,†] and K. V. Adarsh[1,†]

[1]*Department of Physics, Indian Institute of Science Education and Research, Bhopal-462066, India*

[2]*Department of Chemistry, Indian Institute of Science Education and Research, Pune-411008, India*

[3]*Chemistry and Nanoscience Science Center, National Renewable Energy Laboratory, Golden, Colorado 80401, USA*

[4]*Center for Energy Science, Indian Institute of Science Education and Research, Pune-411008, India*

(Received 15 September 2017; revised manuscript received 15 August 2018; published 10 September 2018)

Defect-tolerant perovskite nanocrystals of the general formula Cs-Pb-X_3 (where X = Cl, Br, and I) have shown exceptional potential in fundamental physics as well as in novel optoelectronic applications as the next generation of solar cells. Although exciton many-body interactions such as biexciton Stark shift, state filling, and Auger recombination are studied extensively, other important correlated effects, such as band gap renormalization (BGR) and hot-phonon bottleneck, are not explored in these nanocrystals. Here we experimentally demonstrate the carrier density dependence of the BGR and an effective hot-phonon bottleneck in $CsPb(Cl_{0.20}Br_{0.80})_3$ mixed-halide nanocrystals. The results are compared with two other halide compositions, namely, $CsPbBr_3$ and $CsPb(Br_{0.55}I_{0.45})_3$ nanocrystals with varying band gaps. The optical response of the nanocrystals changes dramatically across the spectral range of many hundreds of meV at high carrier density due to large BGR. We have calculated the BGR constant $\approx(6.0 \pm 0.3) \times 10^{-8}$ eV cm for $CsPb(Cl_{0.20}Br_{0.80})_3$ nanocrystals that provides the amount of band gap shift as a function of carrier density. In these nanocrystals, an efficient hot-phonon bottleneck is observed at a carrier density of $3.1 \times 10^{17}\,cm^{-3}$ that slows down the thermalization by 1 order of magnitude. Our findings reveal that the complex kinetic profile of the exciton dynamics can be analyzed by the global target analysis using the sequential model with increasing lifetimes.

DOI: 10.1103/PhysRevB.98.115418

I. INTRODUCTION

Hybrid organic-inorganic perovskites of the general formula $APbX_3$, where A and X are organic cation and halogen anion, respectively, have led to prototype solar cells with photoconversion efficiencies above 22% [1] from a cost-effective solution processing thin-film synthesis. Although such polycrystalline perovskite thin films have a considerable number of defects at the crystalline boundaries and interfaces, they exhibit exceptionally long carrier lifetimes (microseconds) with resulting carrier diffusion lengths of about $\sim 1\ \mu$m [2]. There is increasing evidence that the low recombination rates of these hybrid perovskites originate from an unusually strong coupling between the electron dynamics and the change in structure due to the rotation of the organic cation [3]. This means that a charge carrier moving through the lattice experiences a dynamical and responsive potential. In other words, the static band-structure picture of standard semiconductors cannot fully explain the electronic properties of the hybrid perovskites. Motivated by the success of thin-film hybrid organic-inorganic perovskites [4], much more stable all-inorganic metal halide colloidal nanocrystals of the formula $CsPbX_3$ exhibiting similar kinds of optoelectronic properties are being studied [5,6]. These $CsPbX_3$ nanocrystals exhibit exciting features such as high photoluminescence (PL) quantum yield (QE) [6,7], reduced PL blinking [8], and high carrier mobility within a nanocrystal measured using terahertz spectroscopy [9]. The long lifetimes of the carriers in these nanocrystals are also attributed to their defect-tolerant nature [10], meaning the energy levels of the defects are not deep within the band gap. Consequently, carrier trapping is considerably reduced and results in a variety of exotic excited states. Moreover, $CsPbX_3$ nanocrystals have been used for various optical and optoelectronic applications, including low-threshold lasing [11], light-emitting diodes [12,13], and solar cells [14]. All these applications primarily rely on the nature of the bound electron-hole pair known as an exciton, typically generated by the absorption of a photon with energy greater than the band gap.

Ultrafast transient absorption (TA) spectroscopy is an important tool to study the exciton dynamics and the many-body interactions in colloidal $CsPbX_3$ nanocrystals [15–17]. Depending on the average number of excitons per nanocrystal $\langle N \rangle$, they exhibit qualitatively different spectral and temporal features of exciton many-body interactions such as the biexciton effect, state filling, and Auger recombination [18,19]. Biexcitons are two neutral bound excitons redshifted by Coulomb fields [20,21]. For instance, $CsPbBr_3$, $CsPb(Br/I)_3$, and $CsPbI_3$ nanocrystals have a biexciton interaction energy of 30–100 meV [18]. The state filling is another important correlated effect in which the occupied excitons at the band edges

*A.M. and J.A. contributed equally to this paper.

†Authors to whom correspondence should be addressed: angshuman@iiserpune.ac.in; adarsh@iiserb.ac.in

block the transition of another exciton by Pauli's exclusion principle [22]. Aneesh *et al.* and Makarov *et al.* observed a pronounced bleach signal at the positions of the first resonant exciton absorption due to state filling in $CsPbX_3$ nanocrystals [19,21]. Nonradiative Auger recombination is another many-body correlated effect in which the exciton transfers energy to a third particle that is reexcited to the higher energy state and dominates the decay of multiexcitons of $CsPbX_3$ nanocrystals of comparable sizes [21]. Similar kinds of ultrafast studies have also been carried out in organic-inorganic hybrid perovskite nanocrystals [23,24].

Despite the extensive research activity on characterizing biexciton, state filling, and Auger recombination in $CsPbX_3$ nanocrystals by TA spectroscopy, quantitative understanding of other excitonic many-body interactions like band gap renormalization (BGR) and hot-phonon bottleneck are still lacking. In this manuscript, we quantitatively discern the BGR, carrier temperature, Auger recombination, and demonstrate the interplay between free-carrier-induced bleaching of the excitonic and continuum transitions near the band edge. Three halide compositions of perovskite nanocrystals, namely, $CsPb(Cl_{0.20}Br_{0.80})_3$, $CsPbBr_3$, and $CsPb(Br_{0.55}I_{0.45})_3$, with band gaps in the range of 2.57−2.16 eV, are studied. Representative data for $CsPb(Cl_{0.20}Br_{0.80})_3$ nanocrystals are mainly shown in the manuscript as representative of the other two halide compositions. We experimentally show the carrier density dependence of the BGR with the constant $\gamma = (6.0 \pm 0.3) \times 10^{-8}$ eV cm in $CsPb(Cl_{0.20}Br_{0.80})_3$ nanocrystals and demonstrate deviations of the LO phonon carrier cooling, which establishes the thermal equilibrium and is indicative of a hot-phonon bottleneck. We suggest that the complex kinetic profile of the exciton dynamics can be analyzed with the global target analysis using the sequential model with increasing lifetime.

II. SAMPLE PREPARATION AND PHYSICAL CHARACTERIZATION

Colloidal $CsPbBr_3$ nanocrystals were prepared following the method reported by Protesescu *et al.* [6]. The mixed-halide compositions, $CsPb(Cl_{0.20}Br_{0.80})_3$ and $CsPb(Br_{0.55}I_{0.45})_3$ nanocrystals, were prepared from $CsPbBr_3$ nanocrystals by employing partial anion exchange reactions [25,26]. All three samples were characterized by using powder x-ray diffraction (PXRD), transmission electron microscopy (TEM), and energy-dispersive x-ray analysis (EDAX). The PXRD pattern of Fig. S1 in the Supplemental Material (SM) [27] shows that $CsPb(Cl_{0.20}Br_{0.80})_3$ nanocrystals exhibit crystal structure in between cubic $CsPbCl_3$ and orthorhombic $CsPbBr_3$ nanocrystals, similar to earlier reports [26]. As the halide compositions change to $CsPbBr_3$ and then to $CsPb(Br_{0.55}I_{0.45})_3$, the PXRD peaks systematically shift towards lower 2θ values, signifying an increase in unit-cell volume because of the increase in the size of halide ions. The TEM image of $CsPb(Cl_{0.20}Br_{0.80})_3$ nanocrystals shown in Fig. 1(a) reveals that the nanocrystals exhibit cubelike morphology with average edge length of ∼11 nm. The composition of the perovskite nanocrystals was confirmed by EDAX measurements (Fig. S2 in SM [27]). For all spectroscopic measurements reported here, we have used the nanocrystals dispersed in toluene.

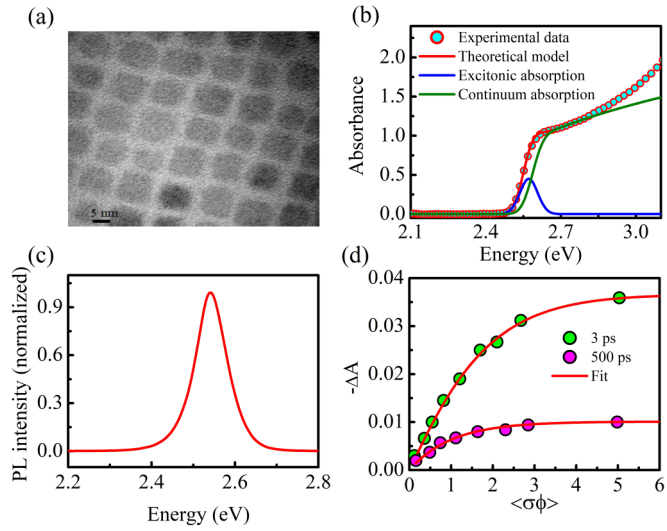

FIG. 1. (a) TEM image of 11-nm $CsPb(Cl_{0.20}Br_{0.80})_3$ nanocrystals. (b) Optical absorption spectrum of $CsPb(Cl_{0.20}Br_{0.80})_3$ nanocrystals together with theoretical fit. (c) Normalized photoluminescence spectrum of colloidal $CsPb(Cl_{0.20}Br_{0.80})_3$ nanocrystals. (d) Optical absorption cross-section calculation from Poisson statistics.

III. RESULTS AND DISCUSSION

A. Optical absorption and emission

The ground-state optical absorption spectrum of $CsPb(Cl_{0.20}Br_{0.80})_3$ nanocrystals shown in Fig. 1(b) demonstrate a sharp exciton band near the direct band gap of the nanocrystals. The excitonic and continuum contributions of the band-edge absorption spectrum are separated by fitting the experimental data using the Elliott equation for a hydrogenic Wannier-Mott exciton model [28]:

$$\begin{aligned}\alpha_T(E) &= \alpha_e(E) + \alpha_c(E) \\ &= \frac{C}{2\pi^2 R_{ex} a_B^3}\left[\sum \frac{4\pi}{n^3}\delta\left(\frac{E-E_g}{R_{ex}} + \frac{1}{n^2}\right)\right. \\ &\quad \left. + \sqrt{\frac{E-E_g}{R_{ex}}}\left(\frac{\frac{2\pi}{l}}{1-e^{-\frac{2\pi}{l}}}\right)\right], \end{aligned} \tag{1}$$

where C, E, E_g, R_{ex}, a_B, and δ are related to the oscillator strength, energy of light, band gap, excitonic Rydberg energy, exciton Bohr radius, and δ function, respectively. Here $l = (\frac{E-E_g}{R_{ex}})^{0.5}$. The first term describes the sharp absorption onset due to the discrete excitonic bound state below the band gap. The second term in Eq. (1) describes the absorption of continuum states, where the right square bracket terms describe the Sommerfeld factor that modifies the above band gap absorption. We modeled the absorption spectrum using an inhomogeneous line-broadening model through convolution of Eq. (1) with a Gaussian function. Details are described in the SM [27]. For photon energies greater than 2.8 eV, the absorption no longer follows Eq. (1) due to the contribution from higher energy bands and does not affect the spectral analysis described in this manuscript. The absorption contributions of the excitonic (blue lines) and continuum (green lines) from the spectral fitting for $CsPb(Cl_{0.20}Br_{0.80})_3$ nanocrystals are shown in Fig. 1(b). From this analysis, we have found that

TABLE I. Band gap (E_g), exciton binding energy (E_b), and center of exciton transition (E_0) for nanocrystals of different compositions.

Sample	E_g (eV)	E_b (meV)	E_0 (eV)
$CsPb(Cl_{0.20}Br_{0.80})_3$	2.59 ± 0.01	20 ± 1	2.57 ± 0.05
$CsPbBr_3$	2.48 ± 0.02	20 ± 1	2.46 ± 0.06
$CsPb(Br_{0.55}I_{0.45})_3$	2.17 ± 0.01	10 ± 0.1	2.16 ± 0.02

the exciton (E_0) and band gap (E_g) of continuum transitions are centered at 2.57 ± 0.05 and 2.59 ± 0.01 eV, respectively. Fitting parameters are tabulated in Table I. Before exploring the exciton many-body interactions of $CsPb(Cl_{0.20}Br_{0.80})_3$ nanocrystals, we have scrutinized the composition-dependent excitonic position and band gap by changing the halogen composition. Typical absorption spectrums of $CsPbBr_3$ and $CsPb(Br_{0.55}I_{0.45})_3$ nanocrystals are shown in the SM (Fig. S3). As shown in Table I, we can observe a consistent redshift of the exciton and band gap energies when the composition is changed from $CsPb(Cl_{0.20}Br_{0.80})_3$ to $CsPb(Br_{0.55}I_{0.45})_3$, and the trend is in accordance with recent reports [6,18,21]. Figure 1(c) shows a strong and narrow (FWHM ~80 meV) excitonic photoluminescence peak at 2.55 eV which exhibits a Stokes shift of ~20 meV from the corresponding excitonic absorption, in agreement with the previous results [26].

B. Poisson statistics and absorption cross section of mixed-halide $CsPb(Cl_{0.20}Br_{0.80})_3$ nanocrystals

We have calculated the average number of excitons per nanocrystal $\langle N \rangle$ by using the equation $\langle N \rangle = \sigma\phi$, where σ and ϕ are optical absorption cross section at the pump beam wavelength and the incident number of photons/cm^2, respectively. To determine σ, we have used femtosecond transient absorption spectroscopy. In our experiment, the nanocrystals were excited by 120-fs pulses of center wavelength 400 nm (above band gap), and a change in absorption of the sample was probed by ultrashort white light pulses (wavelength range 425–750 nm). We have modeled the bleach maxima of the TA at different pump fluences and probe delays using the Poisson distribution, which gives the probability of having nanocrystals with n excitons, $P(n)$ [17,21]:

$$P(n) = \frac{\langle N \rangle^n e^{-\langle N \rangle}}{n!}. \tag{2}$$

We then can define the normalized TA bleach for the biexciton state [17,18,21]

$$-\frac{\Delta A}{A} = P(1) + 2[1 - P(0) - P(1)], \tag{3}$$

where 2 comes from the 2-fold-degenerate band edges [17,21]. From Eq. (2), we can write $P(0) = \exp(-\langle\sigma\phi\rangle)$ and $P(1) = \langle\sigma\phi\rangle \exp(-\langle\sigma\phi\rangle)$, respectively. Then the early time normalized TA for a biexciton can be modeled using Eq. (3) as

$$-\Delta A = A[2 - (2 + \langle\sigma\phi\rangle)e^{-\langle\sigma\phi\rangle}]. \tag{4}$$

Figure 1(d) shows the plot of - ΔA as a function of $\langle\sigma\phi\rangle$ at a delay time of 3 ps, and from the best fit to the data using Eq. (4) we estimate the value of $\sigma = (1.4 \pm 0.1) \times 10^{-14}$ cm^2. Similarly, at a long delay time $t = 500$ ps, when there is only one exciton in the nanocrystals, we can define the amplitude of the transient bleach using the Poisson distribution as

$$-\Delta A = A[1 - e^{-\langle\sigma\phi\rangle}]. \tag{5}$$

By fitting the fluence-dependent TA bleach [Fig. 1(d)], we have accurately determined the value of $\sigma = (1.5 \pm 0.1) \times 10^{-14}$ cm^2 for $CsPb(Cl_{0.20}Br_{0.80})_3$ nanocrystals. The values of σ we calculated using Eqs. (4) and (5) were found to agree with the method discussed in Refs. [26,29,30] and SM [27], and the values are similar to the previous reports [18,19,21]. The values of σ for $CsPbBr_3$ and $CsPb(Br_{0.55}I_{0.45})_3$ nanocrystals are similar to $CsPb(Cl_{0.20}Br_{0.80})_3$ nanocrystals.

C. Exciton many-body interactions and biexciton Stark shift

Figure 2(a) shows the contour plot of the TA spectrum when the $CsPb(Cl_{0.20}Br_{0.80})_3$ nanocrystals sample is excited with the fluence of 14 μJ/cm^2, corresponding to $\langle N \rangle = 0.48$. We have plotted the cross sections of the contour at different probe delays in Fig. 2(b). For subpicosecond pump-probe delay times, the TA spectrum exhibits an asymmetric derivative peak shape with a photoinduced absorption on the lower energy side of the band gap along with a negative signal (photon-induced bleach) on the higher energy side. After 1 ps, the derivative peak shape disappears completely and is replaced with a bleach signal [green and purple circles in Fig. 2(b)]. The spectral characteristics of the early time dynamics indicate that the derivative shape originates from a biexciton state. Thus, at the early time scales, the presence of the pump induces an exciton redshift of δ_{xx} [19,21] which can be used as a sensitive indicator of many-body interactions.

The TA spectrum at different timescales can be modeled accurately by considering the excitonic effect which comes from the biexciton Stark shift due to exciton-exciton interaction and the continuum effects such as redshift in band gap due to band gap renormalization and bleaching of continuum bands (due to state filling) defined by the quasi-Fermi energy. The change in absorbance $\Delta A_{ex}(E, t)$ due to biexciton Stark effect can be written as

$$\Delta A_{ex}(E, t) = A_e e^{-\left(\frac{x - x_0 - \delta_{xx}}{w}\right)^2} - A_g e^{-\left(\frac{x - x_0}{w}\right)^2}, \tag{6}$$

where A, x_0, and w are the amplitude, center of exciton transition, and width, respectively. The subscripts e and g refer to the excited and ground states, respectively. The change in absorbance due to continuum states $\Delta A_{fc}(E)$ can be written [31]

$$\Delta A_{fc}(E) = A_{fc}(E; E_g - \Delta E_g)\left[1 - f_e^q\left(E; E_f^q, T_c\right)\right]^2 - A_{fc}(E, E_g), \tag{7}$$

where $f_e^q(E; E_f^q, T_c)$ is the Fermi-Dirac distribution under excitation characterized by a quasi-Fermi energy E_f^q and a carrier temperature T_c. $A(E, E_g)$ and $A(E; E_g - \Delta E_g)$ are the absorption spectrum before and after BGR. For deriving Eq. (7) we have assumed that $f_e^q \approx f_h^q$ since the electron and hole effective masses are nearly the same for lead halide perovskites [6,32–34]. Then the TA ($\Delta A(E, t)$) spectrum can

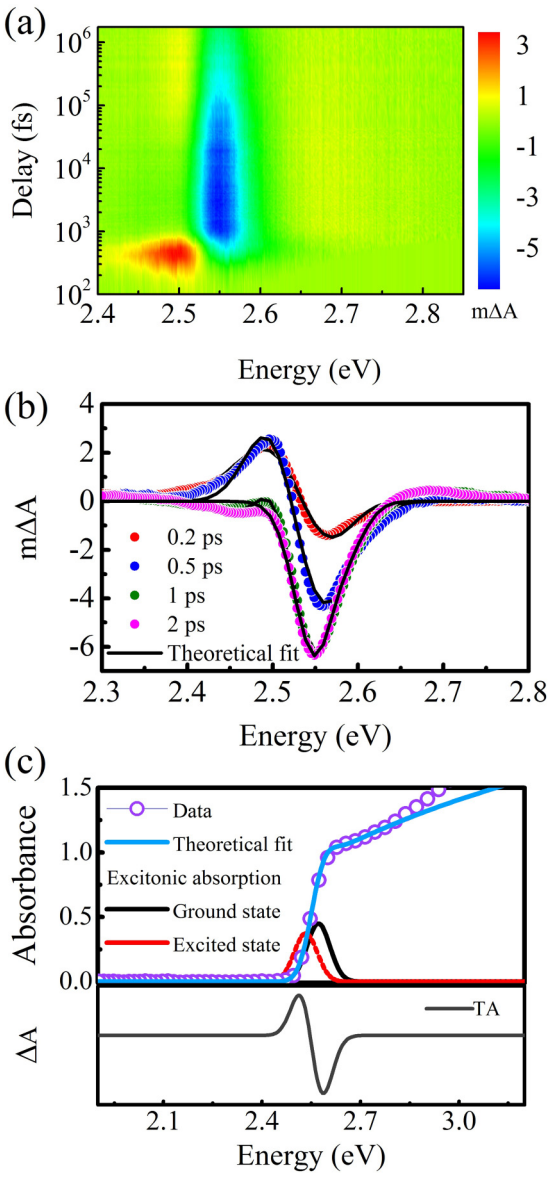

FIG. 2. Data for colloidal $CsPb(Cl_{0.20}Br_{0.80})_3$ nanocrystals. (a) Contour plot of TA at the fluence of 14 $\mu J/cm^2$. (b) Cross sections of contour at different probe delays at a carrier density of 1.8×10^{16} cm^{-3}. Here the solid lines represent the global fit using Eq. (8). (c) Excitonic contribution to the TA spectrum.

be modeled by using Eqs. (6) and (7) such that

$$\Delta A_{ex}(E,t) = A_e e^{-\left(\frac{x-x_0-\delta_{xx}}{w}\right)^2} - A_g e^{-\left(\frac{x-x_0}{w}\right)^2} + A_{fc}(E; E_g - \Delta E_g)\left[1 - f_e^q\left(E; E_f^q, T_c\right)\right]^2 - A_{fc}(E, E_g). \quad (8)$$

Figure 2(b) shows the representative fits using Eq. (8) that match very well to the experimental data for $CsPb(Cl_{0.20}Br_{0.80})_3$ nanocrystals. Similar analyses were carried out for the other two nanocrystal compositions as well, and the best fit parameters are listed in Table II. From the table, we can notice that the value of biexciton Stark shift (δ_{xx}) $= 6 \pm 1$ meV for $CsPb(Cl_{0.20}Br_{0.80})_3$ nanocrystals. It can be seen from Table II that the value of δ_{xx}

TABLE II. Biexciton shift (δ_{xx}) and shift in band gap (ΔE_g) for nanocrystals of different compositions.

Sample	δ_{xx} (meV)[a]	ΔE_g (meV)[a]
$CsPb(Cl_{0.20}Br_{0.80})_3$	6 ± 1	33 ± 2
$CsPbBr_3$	5 ± 1	41 ± 3
$CsPb(Br_{0.55}I_{0.45})_3$	17 ± 1	97 ± 5

[a]Carrier density (cm^{-3}) $= 1.8 \times 10^{16}$ cm^{-3}.

of our $CsPb(Cl_{0.20}Br_{0.80})_3$ nanocrystal is comparable to that of our $CsPbBr_3$ nanocrystals, however slightly lower than $CsPb(Br_{0.55}I_{0.45})_3$ nanocrystals of similar sizes. Further study, with more samples of different compositions, is required for better understanding of the dependence of δ_{xx} on halide compositions of perovskite nanocrystals. The calculated δ_{xx} from our analysis are consistent with the values reported from PL measurements [21]. The excitonic contribution to the TA spectrum is schematically shown in Fig. 2(c).

After $\Delta t > 1$ ps, the asymmetric derivative feature in the TA spectrum disappears completely and shows a strong bleach signal. To explain this effect, we assumed that at the initial times the hot carrier distributions do not occupy the new lowered band edge due to the biexciton effect and hence result in absorption. However, as Δt increases, hot carriers relax into low-energy states of the band edges and lead to state filling [19], which results in bleaching via Pauli blocking. We also assume that exciton and biexciton emissions also contribute to the strong bleach [35], in addition to the state filling that replaces the induced absorption.

D. Continuum bleach and band gap renormalization

The contributions of the continuum (joint density of states with band gap E_g) at an early time of 0.3 ps is schematically represented in Fig. 3(a), which shows the carrier distribution characterized by high temperature (T_c) determined by ($\hbar\omega_{\text{pump}} - E_g$) and quasi-Fermi energy (E_f^q) describing the population of carriers in the valence and conduction bands. The excited carriers created by the pump beam reduce the band gap and redshift the joint density of states, resulting in BGR. The TA spectrum for the continuum states defined by Eq. (7) results in broad bleach, shown in the lower panel of Fig. 3(a). After some time, the carriers undergo thermalization due to inelastic scattering and sharpen the TA as depicted in Fig. 3(b). During this time, we observe a broad absorption feature on the higher energy side (>2.7 eV) termed as photoinduced absorption (PIA).

We have performed a systematic carrier density (n) dependent study to characterize the BGR. Figures 4(a) and 4(b) show the TA spectrum of $CsPb(Cl_{0.20}Br_{0.80})_3$ nanocrystals at two different probe delays indicated in the figure. The TA spectra at 0.3 ps probe delay shown in Fig. 4(a) mainly consist of the asymmetric derivative feature discussed above. It can be noticed from the figure that higher excitation fluence results in the increase in broadening of the absorption and bleach, indicating a large shift in the density of states due to BGR. Another evidence of BGR can be observed from the PIA at the higher energy side (2.7 to 2.8 eV) of Fig. 4(b), where the bleach is replaced with the absorption. This notable

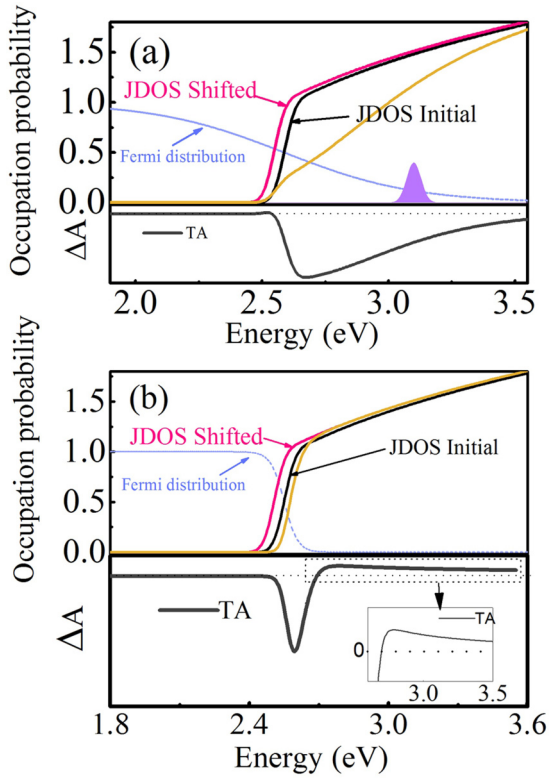

FIG. 3. Data for colloidal $CsPb(Cl_{0.20}Br_{0.80})_3$ nanocrystals. Status of joint density of states and quasi-Fermi level (a) before thermalization and (b) after thermalization. (Lower inset represents the TA bleach for continuum states and lower corner inset represents the photoinduced absorption above 2.6 eV.) Yellow line and violet-filled Gaussian are modified joint density of states and 400-nm pump laser pulse, respectively.

observation primarily comes from the shifted continuum (see Fig. 3). The PIA of the TA spectrum that is not overlapping with the exciton bleach has a $(E)^{-0.5}$ dependence that is indicative of BGR by charge carrier accumulation. Therefore, PIA that significantly changes as a function of carrier density can be better described by

$$PIA(E) = \frac{A \times \Delta E_g}{(E)^{0.5}} = \frac{A \times 2\gamma n^{\frac{1}{3}}}{(E)^{0.5}}, \tag{9}$$

where A, γ, ΔE_g, and n are absorbance, BGR constant, shift in band gap, and carrier density, respectively. By using Eq. (9), we have shown in Fig. 4(c) the linear dependence of ΔE_g on $n^{1/3}$. From the slope of the linear fit, we have estimated the value of $\gamma = (6.0 \pm 0.3) \times 10^{-8}$ eV cm for $CsPb(Cl_{0.20}Br_{0.80})_3$ nanocrystals. PIA onsets of BGR have been observed in $CsPbBr_3$ and $CsPb(Br_{0.55}I_{0.45})_3$ nanocrystals also and the respective values are shown in Table S1 and the fits in Fig. S4 of the SM [27]. From the table, it can be noticed that the γ values are comparable and also similar to bulk lead iodide perovskites [31]. Since γ is related to the band gap (ΔE_g) shifts at higher carrier density, it is an important parameter for applications.

We also observe a broad featureless photoinduced absorption at the lower energy side from 2.1 to 2.4 eV of Fig. 4(a) at higher carrier density ($n = 3.1 \times 10^{17}\,cm^{-3}$). Since the

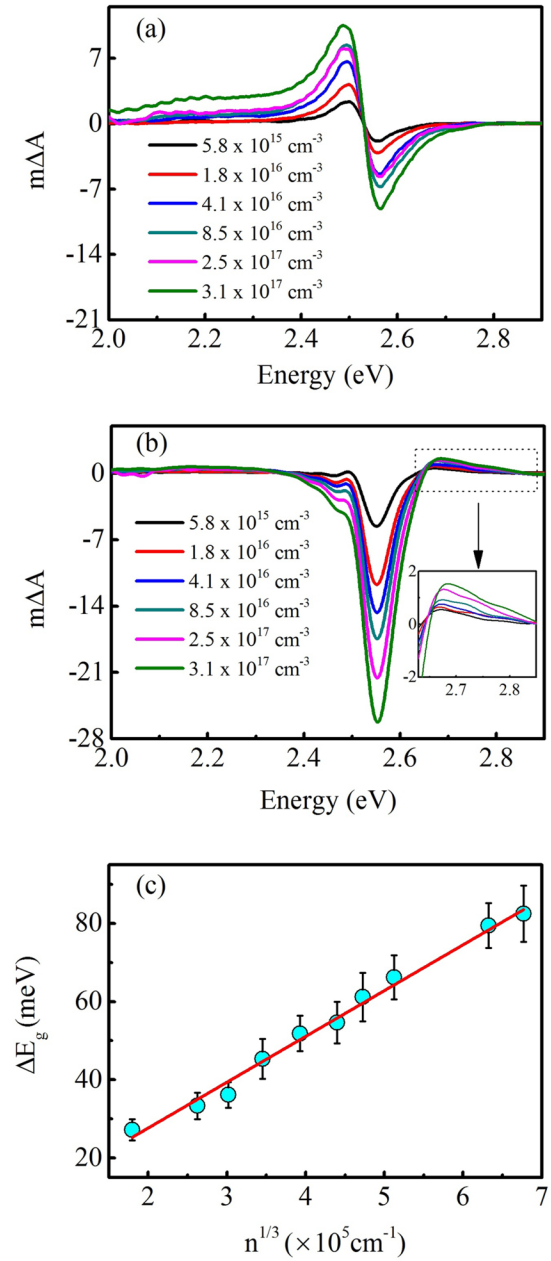

FIG. 4. Data for colloidal $CsPb(Cl_{0.20}Br_{0.80})_3$ nanocrystals. (a,b) Fluence-dependent TA spectrum at 0.3 and 25 ps, respectively. Photoinduced absorption in the lower energy side at higher carrier density is attributed to intraband excited-state absorption. The inset in (b) presents the photoinduced absorption signifying band gap renormalization. (c) Plot of ΔE_g vs $n^{1/3}$ showing band gap renormalization of $CsPb(Cl_{0.20}Br_{0.80})_3$ nanocrystals with a BGR constant of $(6.0 \pm 0.3) \times 10^{-8}$ eV cm.

probe energy in this range certainly cannot invoke interband transitions from the valence band to the conduction band, and since we have not seen the expected Drude free-carrier absorption behavior in which the absorption follows a $(E)^{-2}$ dependence, we assigned this to the intraband transitions of the excited state. A similar broad photoinduced absorption tail has been observed in perovskite nanocrystals [36] and PbI_2 films [37], where it was associated with intraband transitions.

E. Exciton and Auger recombination

The complex kinetic profile of the exciton dynamics is analyzed by the global target analysis using the sequential model with increasing lifetimes. In this model, we globally fitted the decay processes of excitons by a linear combination of three exponentials given by

$$\Delta A(\lambda, t) = i(t) \otimes \sum_{1}^{3} \alpha_l(\lambda) \exp\left(-\frac{t}{\tau_l}\right), \qquad (10)$$

where $i(t)$, $\alpha_l(\lambda)$, τ_1, and $\otimes$ are the instrument response function, amplitude of the exponential decay function, characteristic time constant to decay to $1/e$ of its original value, and the convolution operator, respectively. Figure S5 of the SM [27] shows that three decay constants best fit the cross sections of the contour of $CsPb(Cl_{0.20}Br_{0.80})_3$ nanocrystals with $\langle N \rangle = 0.48$. The three decay constants τ_1, τ_2, and τ_3 are 0.3, 29, and 3100 ps, respectively.

We associate the fast decay constant $\tau_1 = 0.3 \pm 0.2$ ps to the thermalization time for intraband cooling because, within this period, early time band-edge absorption at 2.49 eV is replaced by a strong bleaching at 2.55 eV due to the state filling when carriers relax into the band edges [19]. Therefore, thermalization time can also be determined by fitting the decay of the early time band-edge absorption and the buildup of the band-edge bleach [Fig. 5(a)]. We found that these values exactly match with τ_1.

We have assigned the $\tau_2 = 30 \pm 2$ ps to the lifetime of the biexciton Auger recombination. To ascertain this value to the Auger recombination, we have compared TA decay curves of different pump fluence after normalizing the decay curves so as to match their long-term decay. This procedure is based on the idea that at sufficiently long delay time, there is only a single exciton left in each nanocrystal, and at these time scales, there will be no Auger recombination. Then we followed a simple subtractive procedure discussed in Ref. [38] and fitted the data with a single exponential decay function [Fig. 5(b)]. In this method we have subtracted the TA of $\langle N \rangle = 0.13$ from the trace recorded for $\langle N \rangle > 1$. By fitting the data with a single exponential function, we have observed a pump fluence independent decay constan t $= 29 \pm 2$ ps for $CsPb(Cl_{0.20}Br_{0.80})_3$ nanocrystals, which matches with the value obtained from the global target analysis. Thus we confirm that τ_2 is the lifetime of the biexciton Auger recombination. The biexciton Auger lifetime of our mixed-halide nanocrystal is comparable to that of $CsPbBr_3$ ($\tau_2 = 31 \pm 2$ ps) and $CsPb(Br_{.50}I_{0.45})_3$ ($\tau_2 = 37 \pm 2$ ps) nanocrystals of similar size. Further, fluence-dependent study also revealed the striking evidence that the nanocrystals have only biexciton and single-exciton lifetimes. This observation suggests that the band-edge states are two-fold degenerate [18,21].

We have assigned $\tau_3 = 3100 \pm 50$ ps to the single-exciton lifetime. To prove this, we have measured the lifetime of the exciton bleach maximum at 2.55 eV [Fig. 5(c)] for the lowest excitation fluence ($\langle N \rangle = 0.13$), for which the Auger recombination is negligible. The data is fitted with a single exponential function of decay constant 3030 ± 170 ps. These values are close to the average PL lifetime ($\sim 5100 \pm 110$ ps) shown in Fig. S6 of the SM [27]; however, the slight difference in decay constant of both the methods may be because all

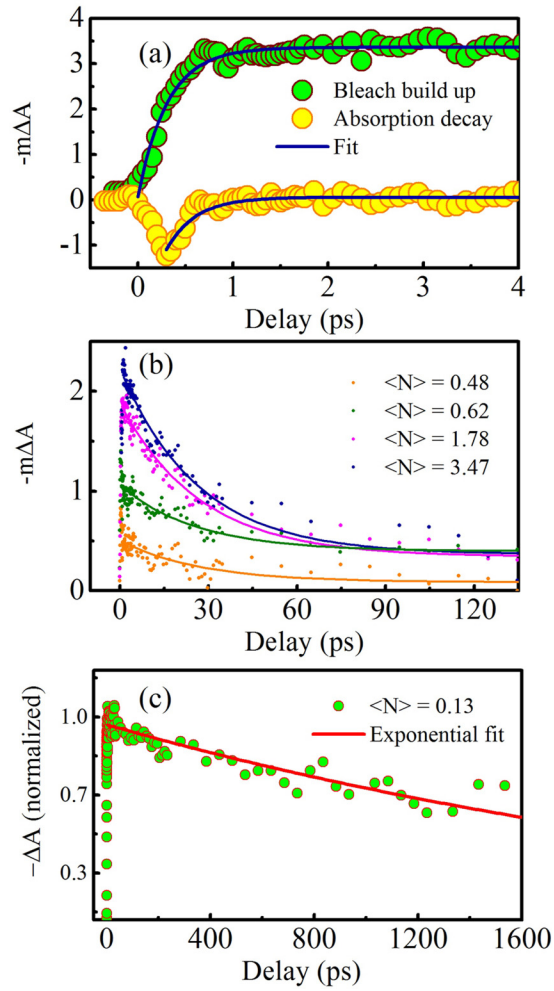

FIG. 5. Data for colloidal $CsPb(Cl_{0.20}Br_{0.80})_3$ nanocrystals. (a) The kinetic traces showing the correlation between the early time absorption at 2.49 eV and bleach at 2.55 eV. The solid lines represent single exponential fit, which gives the intraband cooling time of 0.30 ± 0.02 ps. (b) Pump-fluence-dependent decay kinetics of bleach signal after subtracting the low pump intensity ($\langle N \rangle = 0.13$) from the higher pump fluence ($\langle N \rangle > 1$). (c) Normalized TA data for low pump fluence correspond to $\langle N \rangle = 0.13$. Solid line represents single exponential fit.

nanocrystals in the measured ensemble are characterized by the same radiative decay constant while the nonradiative decay differs among the nanocrystals [21]. Thus, our analysis clearly demonstrates that the complex kinetic profile of the exciton dynamics can be analyzed by the global target analysis using the sequential model with increasing lifetimes. Further, from this analysis we can approximately estimate the population of each process, which is otherwise difficult to estimate from conventional method discussed in Refs. [19] and [21].

F. Thermalization and observation of hot-phonon bottleneck

Another fundamentally important property is the extremely fast intraband relaxation where photogenerated hot carriers dissipate the absorbed optical energy as lattice heat via LO phonon emission [39]. Such processes are influenced by a phonon bottleneck in which the cooling of nonequilibrium hot

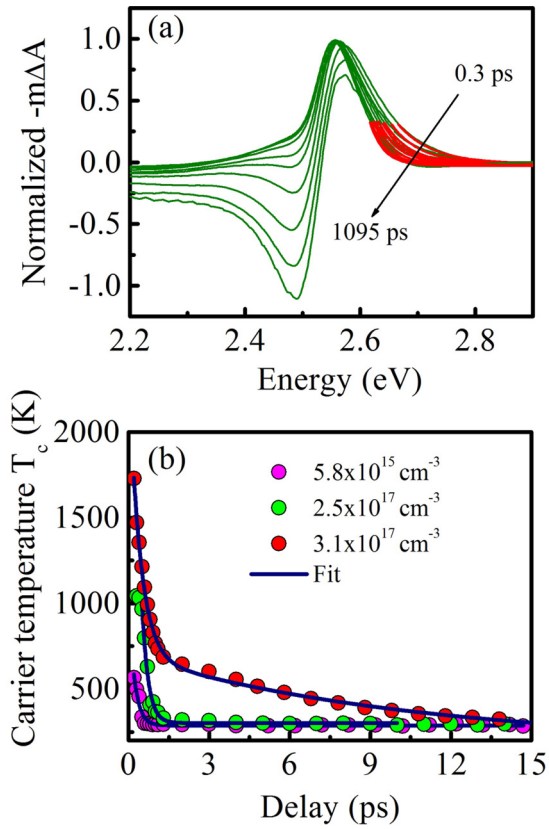

FIG. 6. (a) Normalized negative TA spectrum at different pump-probe delays and (b) thermalization of $CsPb(Cl_{0.20}Br_{0.80})_3$ nanocrystals excited at different carrier densities.

carriers is slowed down at higher excitation fluence (carrier concentrations). Since a phonon bottleneck is desired for photovoltaic applications, we have studied this effect by extracting the carrier temperature (T_c) of nonequilibrium carriers by fitting the higher energy tails of the exciton bleach in the TA. For the hot carriers with energies substantially higher than the Fermi level, the Fermi-Dirac distribution function can, in general, be approximated to a Maxwell-Boltzmann distribution [31,40], which can then be used to extract T_c by fitting the high-energy tail of the TA spectrum [Fig. 6(a)] using the equation

$$\Delta A = A_1 \exp\left(-\frac{E}{k_B T_C}\right), \tag{11}$$

where k_B is the Boltzmann constant and E is the energy $= \hbar\omega$. For calculating T_c, Eq. (11) is then fitted to a high-energy tail of the bleaching spectrum, where the selected tail is from 1/3 of the bleach maximum with a 0.3 eV length (L) along the x axis. (Our selection of this fitting scheme shows reasonably stable and reproducible fitting results under different excitation fluences.)

We first examine the cooling of hot carriers under a low pump excitation fluence of $3.8\,\mu J/cm^2$ that corresponds to $\langle N\rangle = 0.13$ and a carrier density of $5.8 \times 10^{15}\,cm^{-3}$. At such a low carrier density, multiparticle recombination such as Auger recombination is negligible. In Fig. 6(b), we have plotted T_c as a function of probe delay. The average lifetime of the thermalization process is obtained using a single exponential fit with $\tau_1 = 0.3 \pm 0.2$ ps for $CsPb(Cl_{0.20}Br_{0.80})_3$ nanocrystals. Strikingly, when we increased the carrier density to $3.1 \times 10^{17}\,cm^{-3}$, a subsequent slower cooling rate extended to several picoseconds is observed that is a clear indication of a hot-phonon bottleneck [Fig. 6(b)]. At this high carrier density, the average thermalization times are obtained by using a double-exponential fit applied from the initial high carrier temperatures to the end of the cooling curve. Interestingly, the initial rapid cooling rate is independent of fluence and is attributed to the Fröhlich phonon emission, a process where the hot carrier couples to LO phonons to establish a thermal equilibrium [40,41]. After assigning the fast thermalization to the carrier-LO phonon interactions, which governs the carrier relaxation in the first cooling stage, we assigned the slower decay of hot carriers with a lifetime of about 10 ± 1 ps, existing only at higher carrier density of $3.1 \times 10^{17}/cm^3$ to the hot-phonon bottleneck.

IV. CONCLUSIONS

In summary, we have experimentally demonstrated in defect-tolerant cesium lead mixed-halide perovskite nanocrystals that the interplay between the excitonic and continuum transitions near the band edge leads to two important correlated effects: (1) biexciton Stark shift and (2) shift in continuum bands. These correlated effect values of $CsPb(Cl_{0.20}Br_{0.80})_3$ are comparable to those of $CsPbBr_3$, however slightly lower than $CsPb(Br_{0.55}I_{0.45})_3$. Further, detailed studies with more samples of different compositions are required for better understanding of the composition dependence. Carrier thermalization and the hot-phonon bottleneck are studied by extracting the carrier temperatures at different excitation fluences, which revealed an efficient hot-phonon bottleneck at higher carrier densities that slows down the rapid thermalization by an order of magnitude. We suggest that the complex kinetic profile of the exciton dynamics can be analyzed with the global target analysis using the sequential model of three decay constants of increasing lifetimes assigned to thermalization, biexciton nonradiative Auger recombination, and single-exciton decay. Our findings provide a fundamental understanding of the photophysics of perovskite nanocrystals which is crucial for the development of optoelectronics applications, for example, solar cells, light-emitting diodes, and nanocrystal lasers.

ACKNOWLEDGMENTS

The authors gratefully acknowledge the Department of Science and Technology (Project No. EMR/2016/002520) and DAE-BRNS (Project No. 37(3)/14/26/2016-BRNS/37245) for financial support. V.K.S. and W.J.M. acknowledge IISER, Pune, and CSIR, Government of India, respectively, for research fellowships. K.V.A gratefully acknowledges the DST-IUSSTF BASE fellowship. J.A gratefully acknowledges the SERB NPDF fellowship (Sanction Order No. PDF/2017/002048). M.C.B. acknowledges support as part of the Center for Hybrid Organic Inorganic Semiconductors for Energy (CHOISE) an Energy Frontier Research Center funded through the Office of Basic Energy Sciences, Office of

Science within the US Department of Energy (DOE). Support to the National Renewable Energy Laboratory was provided by the DOE under Contract No. DE-AC36-08GO28308. The views expressed in the article do not necessarily represent the views of the DOE or the US Government. The US Government retains and the publisher, by accepting the article for publication, acknowledges that the US Government retains a nonexclusive, paid-up, irrevocable, worldwide license to publish or reproduce the published form of this work, or allow others to do so, for US Government purposes.

[1] W. S. Yang, B.-W. Park, E. H. Jung, N. J. Jeon, Y. C. Kim, D. U. Lee, S. S. Shin, J. Seo, E. K. Kim, and J. H. Noh, Science **356**, 1376 (2017).

[2] Y. Chen, H. T. Yi, X. Wu, R. Haroldson, Y. N. Gartstein, Y. I. Rodionov, K. S. Tikhonov, A. Zakhidov, X.-Y. Zhu, and V. Podzorov, Nat. Commun. **7**, 12253 (2016).

[3] H. Zhu, K. Miyata, Y. Fu, J. Wang, P. P. Joshi, D. Niesner, K. W. Williams, S. Jin, and X.-Y. Zhu, Science **353**, 1409 (2016).

[4] C. X. Sheng, C. Zhang, Y. Zhai, K. Mielczarek, W. Wang, W. Ma, A. Zakhidov, and Z. V. Vardeny, Phys. Rev. Lett. **114**, 116601 (2015).

[5] A. Swarnkar, V. K. Ravi, and A. Nag, ACS Energy Lett. **2**, 1089 (2017).

[6] L. Protesescu, S. Yakunin, M. I. Bodnarchuk, F. Krieg, R. Caputo, C. H. Hendon, R. X. Yang, A. Walsh, and M. V. Kovalenko, Nano Lett. **15**, 3692 (2015).

[7] J. Y. Woo, Y. Kim, J. Bae, T. G. Kim, J. W. Kim, D. C. Lee, and S. Jeong, Chem. Mater. **29**, 7088 (2017).

[8] A. Swarnkar, R. Chulliyil, V. K. Ravi, M. Irfanullah, A. Chowdhury, and A. Nag, Angew Chem. Int. Ed. **54**, 15424 (2015).

[9] G. R. Yettapu, D. Talukdar, S. Sarkar, A. Swarnkar, A. Nag, P. Ghosh, and P. Mandal, Nano Lett. **16**, 4838 (2016).

[10] J. S. Manser, J. A. Christians, and P. V. Kamat, Chem. Rev. **116**, 12956 (2016).

[11] S. Yakunin, L. Protesescu, F. Krieg, M. I. Bodnarchuk, G. Nedelcu, M. Humer, G. De Luca, M. Fiebig, W. Heiss, and M. V. Kovalenko, Nat. Commun. **6**, 8056 (2015)

[12] J. Song, J. Li, X. Li, L. Xu, Y. Dong, and H. Zeng, Adv. Mater. **27**, 7162 (2015).

[13] X. Zhang, H. Lin, H. Huang, C. Reckmeier, Y. Zhang, W. C. H. Choy, and A. L. Rogach, Nano Lett. **16**, 1415 (2016).

[14] A. Swarnkar, A. R. Marshall, E. M. Sanehira, B. D. Chernomordik, D. T. Moore, J. A. Christians, T. Chakrabarti, and J. M. Luther, Science **354**, 92 (2016).

[15] P. Kambhampati, Acc. Chem. Res. **44**, 1 (2011).

[16] R. Sharma, J. Aneesh, R. K. Yadav, S. Sanda, A. R. Barik, A. K. Mishra, T. K. Maji, D. Karmakar, and K. V. Adarsh, Phys. Rev. B **93**, 155433 (2016).

[17] K. Wu, G. Liang, Q. Shang, Y. Ren, D. Kong, and T. Lian, J. Am. Chem. Soc. **137**, 12792 (2015).

[18] J. A. Castañeda, G. Nagamine, E. Yassitepe, L. G. Bonato, O. Voznyy, S. Hoogland, A. F. Nogueira, E. H. Sargent, C. H. B. Cruz, and L. A. Padilha, ACS Nano **10**, 8603 (2016).

[19] J. Aneesh, A. Swarnkar, V. Kumar Ravi, R. Sharma, A. Nag, and K. V. Adarsh, J. Phys. Chem. C **121**, 4734 (2017).

[20] V. Klimov, S. Hunsche, and H. Kurz, Phys. Rev. B **50**, 8110 (1994).

[21] N. S. Makarov, S. Guo, O. Isaienko, W. Liu, I. Robel, and V. I. Klimov, Nano Lett. **16**, 2349 (2016).

[22] D. Huang, J.-I. Chyi, and H. Morkoc, Phys. Rev. B **42**, 5147 (1990).

[23] Y. Hassan, Y. Song, R. D. Pensack, A. I. Abdelrahman, Y. Kobayashi, M. A. Winnik, and G. D. Scholes, Adv. Mater. **28**, 566 (2016)

[24] P. Papagiorgis, L. Protesescu, M. V. Kovalenko, A. Othonos, and G. Itskos, J. Phys. Chem. C **121**, 12434 (2017).

[25] Q. A. Akkerman, V. D'Innocenzo, S. Accornero, A. Scarpellini, A. Petrozza, M. Prato, and L. Manna, J. Am. Chem. Soc. **137**, 10276 (2015).

[26] V. K. Ravi, G. B. Markad, and A. Nag, ACS Energy Lett. **1**, 665 (2016).

[27] See Supplemental Material at http://link.aps.org/supplemental/10.1103/PhysRevB.98.115418 for PXRD and EDAX analysis, optical absorption spectrum, band gap renormalization (BGR) constant calculation, global fitting for the contour at the average exciton density of 0.48, and time-resolved photoluminescence fluorescence spectrum.

[28] R. J. Elliott, Phys. Rev. **108**, 1384 (1957).

[29] Z. Liu, J. A. Peters, C. C. Stoumpos, M. Sebastian, B. W. Wessels, J. Im, A. J. Freeman, and M. G. Kanatzidis, in *Heavy Metal Ternary Halides for Room-Temperature X-ray and Gamma-ray Detection*, edited by M. Fiederle, A. Burger, L. Franks, and R. B. James (San Diego, CA, 2013), p. 88520A.

[30] J. Jasieniak, L. Smith, J. van Embden, P. Mulvaney, and M. Califano, J. Phys. Chem. C **113**, 19468 (2009).

[31] Y. Yang, D. P. Ostrowski, R. M. France, K. Zhu, J. van de Lagemaat, J. M. Luther, and M. C. Beard, Nat. Photonics **10**, 53 (2015).

[32] G. Giorgi, J.-I. Fujisawa, H. Segawa, and K. Yamashita, J. Phys. Chem. Lett. **4**, 4213 (2013).

[33] W.-J. Yin, T. Shi, and Y. Yan, Adv. Mater. **26**, 4653 (2014).

[34] A. Amat, E. Mosconi, E. Ronca, C. Quarti, P. Umari, M. K. Nazeeruddin, M. Grätzel, and F. De Angelis, Nano Lett. **14**, 3608 (2014).

[35] T. S. Bischof, R. E. Correa, D. Rosenberg, E. A. Dauler, and M. G. Bawendi, Nano Lett. **14**, 6787 (2014).

[36] N. Mondal and A. Samanta, Nanoscale **9**, 1878 (2017).

[37] O. Flender, J. R. Klein, T. Lenzer, and K. Oum, Phys. Chem. Chem. Phys. **17**, 19238 (2015).

[38] V. I. Klimov, A. A. Mikhailovsky, D. W. McBranch, C. A. Leatherdale, and M. G. Bawendi, Science **287**, 1011 (2000).

[39] H. Kawai, G. Giorgi, A. Marini, and K. Yamashita, Nano Lett. **15**, 3103 (2015).

[40] J. Yang, X. Wen, H. Xia, R. Sheng, Q. Ma, J. Kim, P. Tapping, T. Harada, T. W. Kee, F. Huang, Y.-B. Cheng, M. Green, A. Ho-Baillie, S. Huang, S. Shrestha, R. Patterson, and G. Conibeer, Nat. Commun. **8**, 14120 (2017).

[41] E. J. Yoffa, Phys. Rev. B **23**, 1909 (1981).